ELSEVIER

Volume 179, Number 12, December 2006

JOURNAL OF SOLID STATE CHEMISTRY

www.elsevier.com/locate/jssc

CONTENTS

Abstracted/indexed in BioEngineering Abstracts, Chemical Abstracts, Coal Abstracts, Current Contents/Physics, Chemical, & Earth Sciences, Engineering Index, Research Alert, SCISEARCH, Science Abstracts, and Science Citation Index. Also covered in the abstract and citation database SCOPUS®. Full text available on ScienceDirect®.

Regular Articles

Hydrothermal synthesis and structure determination of the new vanadium molybdenum mixed oxide $V_{1.1}Mo_{0.9}O_5$ from synchrotron X-ray powder diffraction data
F. Duc, S. Gonthier, M. Brunelli and J.C. Trombe
Page 3591

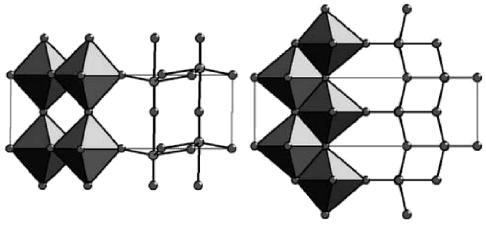

View of the (*a*, *c*) and (*a*, *b*) planes (at left and right side, respectively) of the new vanadium molybdenum mixed oxide $V_{1.1}Mo_{0.9}O_5$.

***In situ* X-ray powder diffraction, synthesis, and magnetic properties of $InVO_3$**
Rylan J. Lundgren, Lachlan M.D. Cranswick and Mario Bieringer
Page 3599

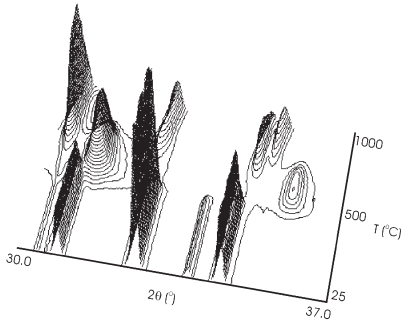

In situ powder X-ray diffractograms for the reduction of $InVO_4$ in CO/CO_2. The three temperature regions show the conversion of $InVO_4$ to $InVO_3$ and final decomposition into In_2O_3 and V_2O_3.

Regular Articles—Continued

The low-temperature form of Rb_2KCrF_6 and Rb_2KGaF_6: The first example of an elpasolite-derived structure with pentagonal bipyramid in the B-sublattice
Francisco Javier Zúñiga, Alain Tressaud and Jacques Darriet
Page 3607

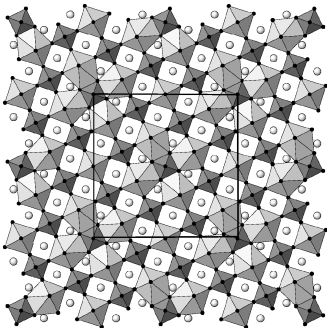

Section at $z = 0$ of the structure of the low temperature form of Rb_2KMF_6 (M = Cr, Ga) showing the pentagonal bipyramids.

Synthesis and characterization of two new photochromic organic–inorganic hybrid materials based on isopolyoxomolybdate: $(HDBU)_3(NH_4)[\beta\text{-}Mo_8O_{26}]\cdot H_2O$ and $(HDBU)_4[\delta\text{-}Mo_8O_{26}]$
Violaine Coué, Rémi Dessapt, Martine Bujoli-Doeuff, Michel Evain and Stéphane Jobic
Page 3615

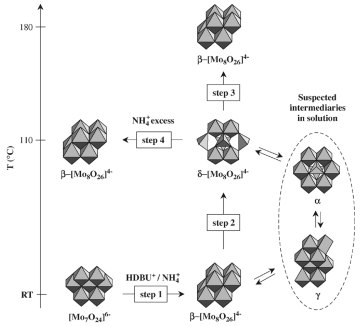

Schematic representation of the thermal and chemical isomerizations of the two $[Mo_8O_{26}]^{4-}$ observed in $(HDBU)_3(NH_4)[\beta\text{-}Mo_8O_{26}]\cdot H_2O$ and $(HDBU)_4[\delta\text{-}Mo_8O_{26}]$.

A hybrid material based on $[Mo_6Br_{14}]^{2-}$ inorganic cluster units and $[BEDO\text{-}TTF]^{+}$ organic monocationic radicals: Synthesis, structure and properties of $(BEDO\text{-}TTF)_2Mo_6Br_{14}(PhCN)_4$

Kaplan Kirakci, Hidemasa Hosoda, Stéphane Cordier, Christiane Perrin and Gunzi Saito

Page 3628

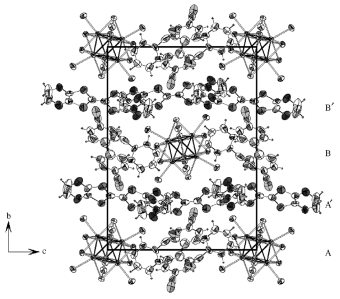

The structure of $(BEDO\text{-}TTF)_2Mo_6Br_{14}(PhCN)_4$ is built up from a $[BEDO\text{-}TTF]^{+}$ and PhCN organic framework in which are hosted $[Mo_6Br_{14}]^{2-}$ inorganic cluster units.

The intergrowth structure of $Ag_{1.2}Bi_{17.6}S_{23}Cl_8$ and its relation to the tubular structure of $Bi_{6+\delta}S_{6+3\delta}Cl_{6-3\delta}$ and the pavonite homologue $Ag_{3x}Bi_{5-3x}S_{8-6x}Cl_{6x-1}$

Pierre F.P. Poudeu and Michael Ruck

Page 3636

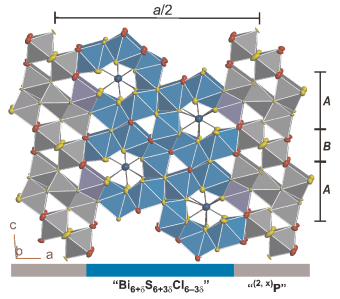

The intergrowth structure of $Ag_{1.2}Bi_{17.6}S_{23}Cl_8$ highlighting the two alternating types of structural units.

Differences on the conversion of celestite in solutions bearing monovalent ions under hydrothermal conditions

J.C. Rendón-Angeles, M.I. Pech-Canul, J. López-Cuevas, Z. Matamoros-Veloza and K. Yanagisawa

Page 3645

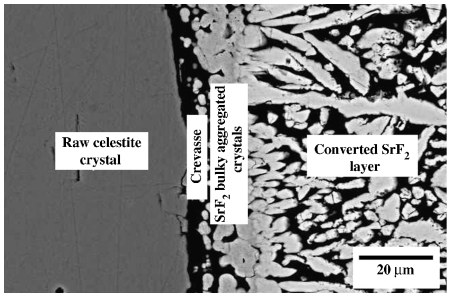

Typical SEM image of the reaction interface determined on partially converted $SrSO_4$ crystals obtained at 250 °C after 6 h in an NaF solution with a F^-/SO_4^{2-} molar ratio = 10.

Syntheses, structures, and vibrational spectroscopy of the two-dimensional iodates $Ln(IO_3)_3$ and $Ln(IO_3)_3(H_2O)$ (Ln = Yb, Lu)

Zerihun Assefa, Jie Ling, Richard G. Haire, Thomas E. Albrecht-Schmitt and Richard E. Sykora

Page 3653

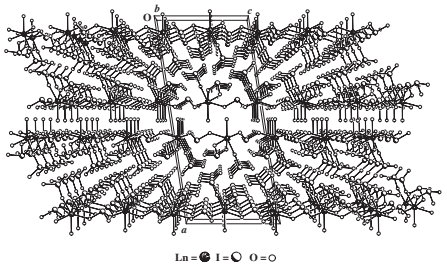

Four new metal iodates, $Yb(IO_3)_3$, $Lu(IO_3)_3$, $Yb(IO_3)_3(H_2O)$, and $Lu(IO_3)_3(H_2O)$, have all been isolated as single crystals through the use of hydrothermal reactions. Structural determinations using single-crystal X-ray diffraction have shown that the materials are all alike in that they contain two-dimensional structures. Vibrational profiles for all of the materials have been collected using Raman spectroscopy and analyzed.

Synthesis and crystal structure of three silver indium double phosphates

M.A. Strelkov, M.G. Zhizhin and L.N. Komissarova

Page 3664

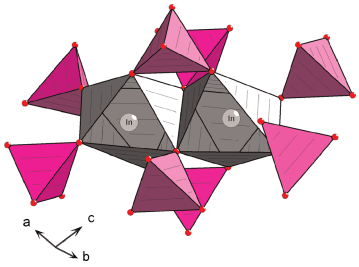

The dimer block In_2O_{10} with PO_4-tetrahedra in α-$Ag_3In_2(PO_4)_3$.

Synthesis, crystal structure and magnetic properties of new indium rhenium and scandium rhenium oxides, In_6ReO_{12} and Sc_6ReO_{12}

D. Mikhailova, H. Ehrenberg and H. Fuess

Page 3672

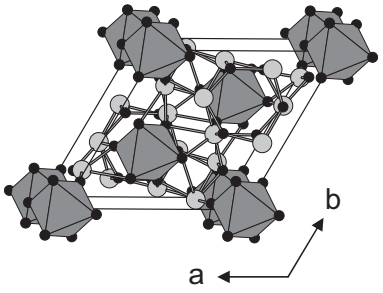

Crystal structure of M_6ReO_{12} (M = In, Sc) showing the distribution of ReO_6 octahedra and M^{3+} cations in the unit cell.

Continued

A crystal structure of mixed-metal dianionic phosphate $Cs_{3.70}Mg_{0.60}Ti_{2.78}(TiO)_3(P_2O_7)_4(PO_4)_2$
Ivan V. Ogorodnyk, Igor V. Zatovsky, Nikolay S. Slobodyanik, Vyacheslav N. Baumer and Oleg V. Shishkin
Page 3681

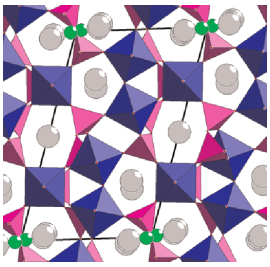

Projection of $Cs_{3.70}Mg_{0.60}Ti_{2.78}(TiO)_3(P_2O_7)_4(PO_4)_2$ on the *bc* plane.

Distinct host–guest interaction and subdued fluorescence in a coordination network of 2,3,6,7,10,11-hexakis(phenylthio)triphenylene and silver(I) triflate
Kunhao Li, Guo Huang, Zhengtao Xu and Patrick J. Carroll
Page 3688

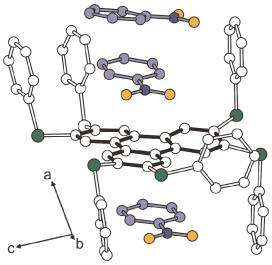

Well-defined host–guest interactions are observed and apparently lead to subdued fluorescence in a coordination network of 2,3,6,7,10,11-hexakis(phenylthio)triphenylene and silver(I) triflate.

Heterobimetallic thiocyanato-bridged coordination polymers based on $[Hg(SCN)_4]^{2-}$: Synthesis, crystal structure, magnetic properties and ESR studies
Fang-Fang Jian, Hai-Lian Xiao and Fa Qian Liu
Page 3695

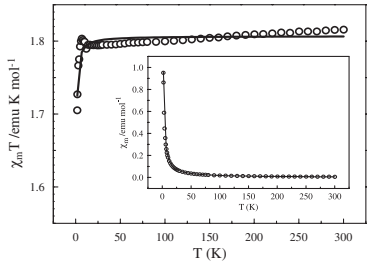

Three new *M*/Hg bimetallic thiocyanato-bridged coordination polymers; $[Hg(SCN)_4Ni(Im)_3]_\infty$ **1**, $[Hg(SCN)_4Mn(Im)_2]_\infty$ **2**, and $[Hg(SCN)_4Cu(Me–Im)_2\ Hg(SCN)_4Cu(Me–Im)_4]_\infty$ **3**, (Im = imidazole, Me–Im = *N*-methyl-imidazole), have been synthesized and characterized by single-crystal X-ray. All coordination polymers possess 3-D structures, and consist of organic base neutral ligands (imidazole and *N*-methyl-imidazole) and SCN^{-1} anions. Their structural difference is mainly caused by the role of the organic base and metal ions. The complex **1** shows the irregular spin state structure.

Electronic structure and visible light photocatalysis water splitting property of chromium-doped $SrTiO_3$
J.W. Liu, G. Chen, Z.H. Li and Z.G. Zhang
Page 3704

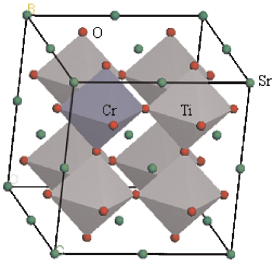

$SrTi_{1-x}Cr_xO_3$ powders, prepared by solvothermal method, can absorb not only UV light like pure $SrTiO_3$ powder but also the visible-light spectrum ($\lambda > 420$ nm). The results of DFT calculation illuminate that the visible-light absorption bands in the $SrTi_{1-x}Cr_xO_3$ catalyst are attributed to the band transition from the Cr 3*d* to the Cr 3*d* + Ti 3*d* hybrid orbital.

Synthesis, structure, magnetic susceptibility and Mössbauer and Raman spectroscopies of the new oxyphosphate $Fe_{0.50}TiO(PO_4)$
S. Benmokhtar, A. El Jazouli, J.P. Chaminade, P. Gravereau, A. Wattiaux, L. Fournès, J.C. Grenier and D. Waal
Page 3709

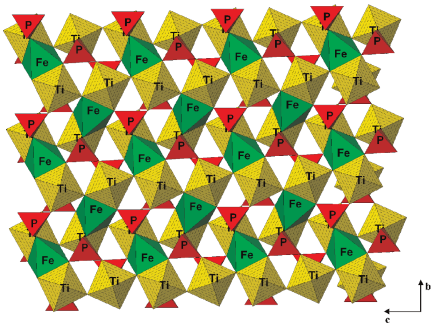

A polyhedral view of framework as projected in the (b, c) plane.

Investigation of luminescence and optical absorption of $K_2LiAlF_6:Cr^{3+}$ single crystals
M.A.F.M. da Silva, R.B. Barthem and L.P. Sosman
Page 3718

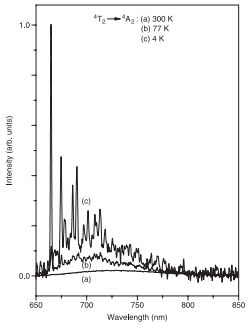

Photoluminescence spectra of K_2LiAlF_6 doped with 1.0 at% Cr^{3+} at: (a) room temperature (300 K), (b) 77 K and (c) 4 K.

A novel cesium hydroxygallophosphate with a layered structure built up of rutile ribbons: $CsGa_2(OH)_2[(PO_4)H(PO_4)]$
J. Lesage, A. Guesdon and B. Raveau
Page 3724

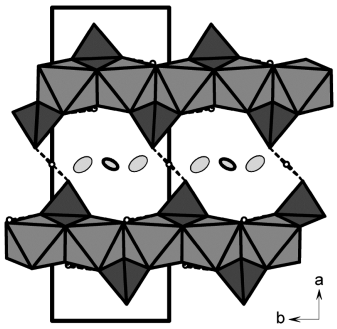

View along ***c*** of the 2D structure of $CsGa_2(OH)_2[(PO_4)H(PO_4)]$ exhibiting strong symmetric hydrogen bonds in dashed lines.

Energetics of cobalt phosphate frameworks: α, β, and red $NaCoPO_4$
So-Nhu Le, Hank W. Eng and Alexandra Navrotsky
Page 3731

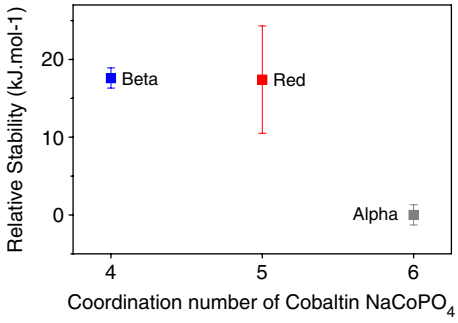

Relative stability of $NaCoPO_4$ polymorphs compared to the most stable phase, α $NaCoPO_4$.

Dielectric properties of $Ca(Zr_{0.05}Ti_{0.95})O_3$ thin films prepared by chemical solution deposition
L.S. Cavalcante, A.Z. Simões, L.P.S. Santos, M.R.M.C. Santos, E. Longo and J.A. Varela
Page 3739

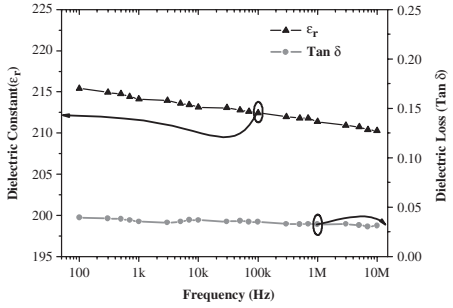

Dielectric constant and dielectric loss of the CZT thin film dependent of the applied frequency.

Synthesis and structural studies of cation-substituted Aurivillius phases $ASrBi_2Nb_2TiO_{12}$
Qingdi Zhou, Brendan J. Kennedy and Margaret M. Elcombe
Page 3744

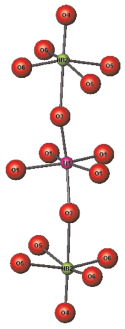

Details of the coordination environment of the Nb and Ti atoms.

Thermoelectric properties of p-type pseudo-binary $(Ag_{0.365}Sb_{0.558}Te)_x$–$(Bi_{0.5}Sb_{1.5}Te_3)_{1-x}$ ($x = 0$–1.0) alloys prepared by spark plasma sintering
J.L. Cui, H.F. Xue, W.J. Xiu, L. Jiang and P.Z. Ying
Page 3751

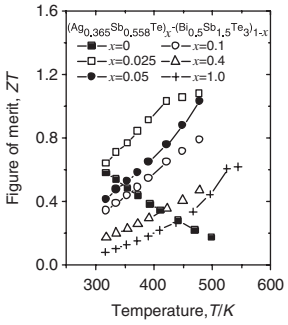

The temperature dependence of the dimensionless thermoelectric figure of merit ZT for different $(Ag_{0.365}Sb_{0.558}Te)_x$–$(Bi_{0.5}Sb_{1.5}Te_3)_{1-x}$ ($x = 0$–1.0) alloys prepared by spark plasma sintering.

A facile high-yield solvothermal route to tin phosphide Sn_4P_3
Kirill A. Kovnir, Yury V. Kolen'ko, Sugata Ray, Jinwang Li, Tomoaki Watanabe, Mitsuru Itoh, Masahiro Yoshimura and Andrei V. Shevelkov
Page 3756

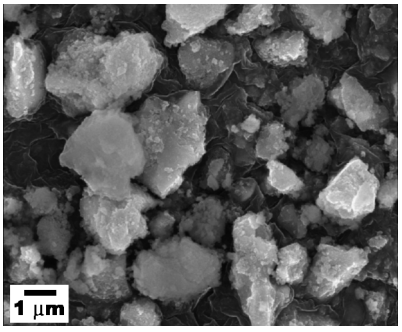

SEM microphotograph of the sample of layered tin phosphide Sn_4P_3, which can be simply solvothermally synthesized from metallic tin and red phosphorus.

Continued

Crystal structure and magnetic properties of the coupled spin dimer compound $SrCu_2(TeO_3)_2Cl_2$
Rie Takagi, Mats Johnsson, Reinhard K. Kremer and Peter Lemmens
Page 3763

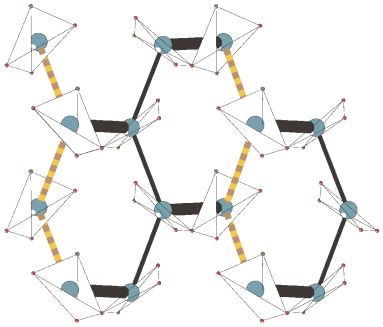

Corner sharing CuO_3Cl and CuO_4 square-planes result in strongly coupled Cu–Cu dimers that are connected by weaker couplings to form a distorted honeycomb pattern of Cu atoms.

Partial exchange of the Li^+, Na^+ and K^+ alkaline cations in the $HNi(PO_4)\cdot H_2O$ layered compound
Jaione Escobal, José Mesa, José Pizarro, Begoña Bazan, María Arriortua and Teófilo Rojo
Page 3768

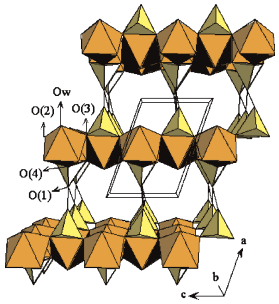

Layered crystal structure of $HNi(PO4)\cdot H_2O$.

Structure and physical properties of rare-earth zinc antimonides $RE Zn_{1-x}Sb_2$ (RE = La, Ce, Pr, Nd, Sm, Gd, Tb)
Oksana Ya. Zelinska and Arthur Mar
Page 3776

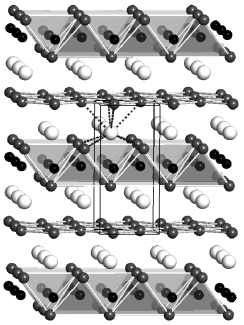

$RE Zn_{1-x}Sb_2$ ($HfCuSi_2$-type) exhibits deficiencies in the tetrahedral Zn sites. Electrical and magnetic properties have been measured for different RE members.

Microwave-treated layered double hydroxides containing Ni^{2+} and Al^{3+}: The effect of added Zn^{2+}
P. Benito, F.M. Labajos and V. Rives
Page 3784

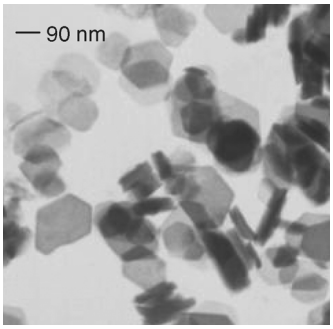

Layered double hydroxides were prepared by the microwave-hydrothermal treatment. This method allows obtaining in short periods of time well crystallized LDHs with well-defined hexagonal-shaped particles, and improved thermal stability and the textural properties. In addition, the degree of crystallinity of the layered precursors and their textural properties determine the properties of their thermal decomposition products.

Energetics of charge order transition in $Bi_{1-x}Sr_xMnO_3$
D. Sedmidubský, A. Strejc, O. Beneš, K. Ružička, J. Hejtmánek, P. Javorský, M. Nevřiva and C. Martin
Page 3798

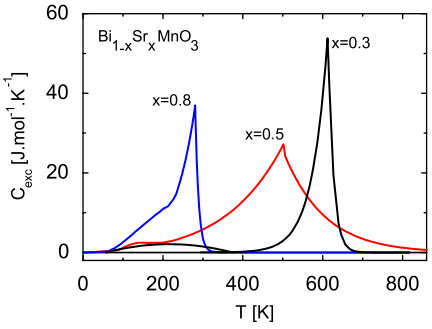

$Bi_{1-x}Sr_xMnO_3$-heat capacity of charge/orbital and magnetic ordering transition.

Structural manipulation of pyrochlores: Thermal evolution of metastable $Gd_2(Ti_{1-y}Zr_y)_2O_7$ powders prepared by mechanical milling
Karla J. Moreno, Antonio F. Fuentes, Miroslaw Maczka, Jerzy Hanuza and Ulises Amador
Page 3805

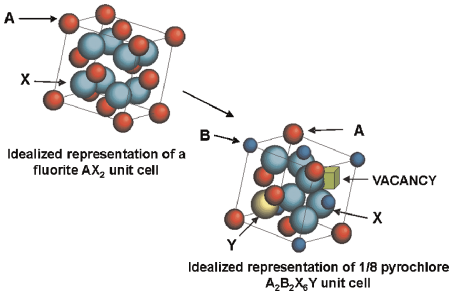

Phase transition on metastable $Gd_2(Ti_{0.65}Zr_{0.35})_2O_7$ powders.

V_2O_5 xerogel–poly(ethylene oxide) hybrid material: Synthesis, characterization, and electrochemical properties
Elidia M. Guerra, Kátia J. Ciuffi and Herenilton P. Oliveira
Page 3814

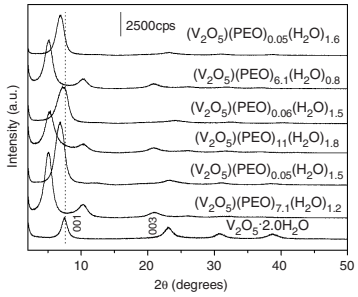

The synthesis, structural and electrochemical properties of vanadium pentoxide xerogel–poly(ethylene oxide) hybrid materials have been described. Despite the presence of broad and low intensity peaks, the X-ray diffractograms indicate that the lamellar structure of the vanadium pentoxide xerogel is preserved. The cyclic voltammetry technique demonstrated that PEO intercalation provides an improvement in the electrochemical properties, mainly with respect to the lithium electroinsertion process into the oxide matrix.

Synthesis and structure of $In(IO_3)_3$ and vibrational spectroscopy of $M(IO_3)_3$ (M = Al, Ga, In)
Nhan Ngo, Katrina Kalachnikova, Zerihun Assefa, Richard G. Haire and Richard E. Sykora
Page 3824

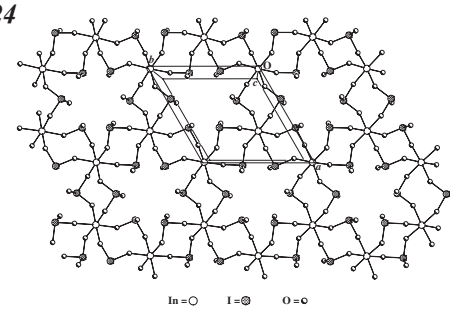

$Al(IO_3)_3$, $Ga(IO_3)_3$, and $In(IO_3)_3$ have been prepared by reacting the appropriate group 13 metal with H_5IO_6 in aqueous media at 180 °C. Single-crystal X-ray diffraction has shown that $In(IO_3)_3$ contains the Te_4O_9-type structure in contrast to the $Fe(IO_3)_3$-type structure observed previously for $Al(IO_3)_3$ and $Ga(IO_3)_3$. Raman spectra reveal that $Al(IO_3)_3$ and $Ga(IO_3)_3$ show similar vibrational profiles due to their isostructural nature, but $In(IO_3)_3$ has been found to display a distinctively different vibrational profile. Therefore, Raman spectroscopy can be used as a rapid diagnostic tool to discern the different structural motifs of these two-structure types.

Comparative study of $LiMn_2O_4$ thin film cathode grown at high, medium and low temperatures by pulsed laser deposition
S.B. Tang, M.O. Lai, L. Lu and S. Tripathy
Page 3831

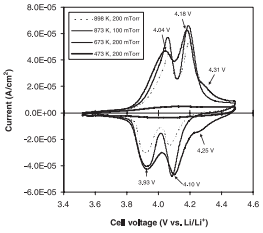

$LiMn_2O_4$ thin films with different crystal size were grown at high, medium and low temperatures by PLD. Cyclic voltammograms of $LiMn_2O_4$ thin film electrodes deposited at different temperatures show that the excellent performance of nano-crystalline film was correlated to its microstructures.

High-pressure growth of $NaMn_7O_{12}$ crystals
Edi Gilioli, Gianluca Calestani, Francesca Licci, Carlo Paorici, Andrea Gauzzi, Fulvio Bolzoni and Andrea Prodi
Page 3839

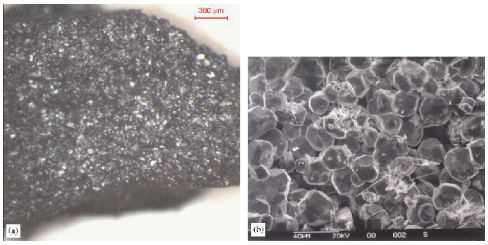

Optical (a) and SEM images (b) of $NaMn_7O_{12}$ crystals. Note the markers: 300 μm, top-right corner (a) and 40 μm, bottom left (b).

Disordered commensurate structure of the 2212-related phase $Fe_2(Bi_{0.69}Sr_{2.31})Fe_2O_{9.5\pm1/2\delta}$ and structural mechanism
Dominique Grebille, Christophe Lepoittevin, Sylvie Malo, Oliver Pérez, N. Nguyen and Maryvonne Hervieu
Page 3849

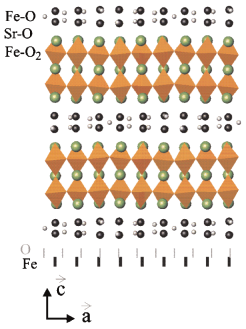

Schematic representation of the structure projected along **b**. The average periodicity of the Fe and O atoms in the rock salt-type layers is shown.

Unit-cell intergrowth of pyrochlore and hexagonal tungsten bronze structures in secondary tungsten minerals
Ian E. Grey, William D. Birch, Catherine Bougerol and Stuart J. Mills
Page 3860

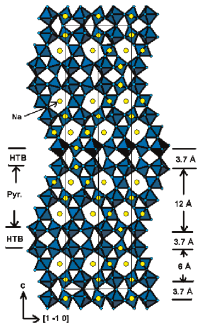

Polyhedral representation of the structure of pittongite viewed along [110].

Continued

Crystal structures and phase transitions of $SrZr(PO_4)_2$–$BaZr(PO_4)_2$ solid solutions
Koichiro Fukuda, Tomoyuki Iwata, Akira Moriyama and Shinobu Hashimoto
Page 3870

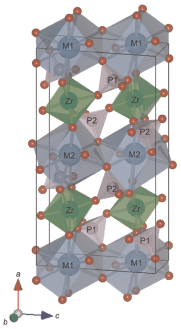

Crystal structure of $Sr_{0.7}Ba_{0.3}Zr(PO_4)_2$.

Synthesis and crystal structure of gallosilicate- and aluminogermanate tetrahydroborate sodalites $Na_8[GaSiO_4]_6(BH_4)_2$ and $Na_8[AlGeO_4]_6(BH_4)_2$
Josef-C. Buhl, Thorsten M. Gesing, Tanja Höfs and Claus H. Rüscher
Page 3877

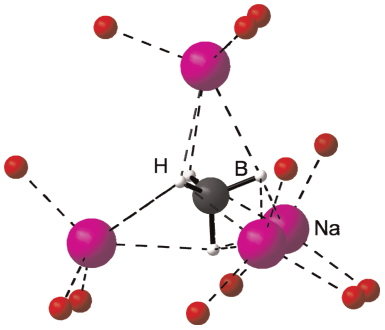

Coordination of the non-framework atoms in the gallosilicate tetrahydroborate sodalite together with three oxygen atoms of the framework around each sodium atom.

Ag_2CuMnO_4: A new silver copper oxide with delafossite structure
David Muñoz-Rojas, Gloria Subías, Judith Oró-Solé, Jordi Fraxedas, Benjamín Martínez, Montse Casas-Cabanas, Jesús Canales-Vázquez, Jose Gonzalez-Calbet, Ester García-González, Richard I. Walton and Nieves Casañ-Pastor
Page 3883

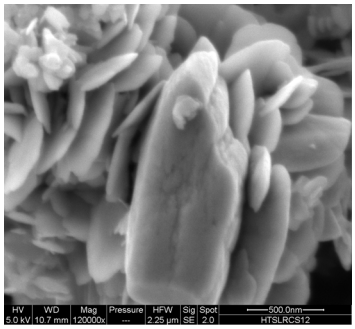

Ag_2CuMnO_4 platelet.

Synthesis and high-temperature thermoelectric properties of Ni and Ti substituted $LaCoO_3$
R. Robert, L. Bocher, M. Trottmann, A. Reller and A. Weidenkaff
Page 3893

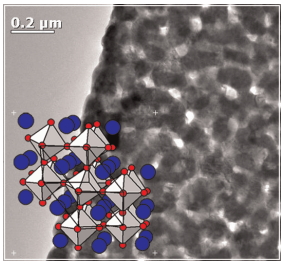

The three parameters defining the thermoelectric figure of merit are interdependent. As e.g. the thermopower increases so does the resistivity. Therefore, an optimum charge carrier concentration and mobility has to be defined in rhombohedral thermoelectric cobaltate structures. The heat conductivity can be lowered by enhanced boundary scattering in nanostructured materials without changing the electronic transport.

Phase formation, crystal chemistry, and properties in the system Bi_2O_3–Fe_2O_3–Nb_2O_5
Michael W. Lufaso, Terrell A. Vanderah, Ileana M. Pazos, Igor Levin, Robert S. Roth, Juan C. Nino, Virgil Provenzano and Peter K. Schenck
Page 3900

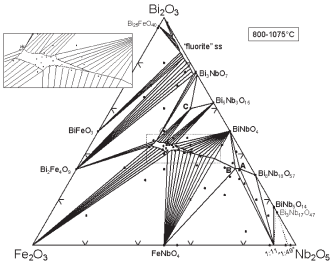

Raman scattering spectra at room temperature for A: 60 KTG glass, B: crystallized (644 °C, 3 h) sample of KTG glass, and C: $K_2TiGe_3O_9$ crystalline phase prepared by a solid state reaction. 60 KTG: $20K_2O$–$20TiO_2$–$60GeO_2$.

Syntheses and crystal structures of two new hydrated borates, $Zn_8[(BO_3)_3O_2(OH)_3]$ and $Pb[B_5O_8(OH)] \cdot 1.5H_2O$
Xuean Chen, Yinghua Zhao, Xinan Chang, Jianlong Zuo, Hegui Zang and Weiqiang Xiao
Page 3911

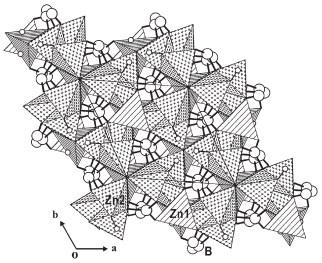

$Zn_8[(BO_3)_3O_2(OH)_3]$ represents a new structure type in which Zn-centered tetrahedra are connected via common vertices to form a three-dimensional framework. The boron atoms are incorporated into the channels in the framework to strengen the structure via B–O bonds. $Pb[B_5O_8(OH)] \cdot 1.5H_2O$ is a new layered material containing double ring $[B_5O_8(OH)]^{2-}$ building units that share exocyclic oxygen atoms to form a two-dimensional layer.

Crystal structures and photocatalysis of the triclinic polymorphs of $BiNbO_4$ and $BiTaO_4$
B. Muktha, J. Darriet, Giridhar Madras and T.N. Guru Row
Page 3919

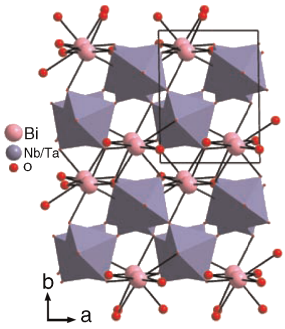

Crystal structures of $Bi(Nb/Ta)O_4$ along *b*-axis: triclinic form.

Metal dicyanamide layered coordination polymers with cyanopyridine co-ligands: Synthesis, crystal structures and magnetism
Miao Du, Qian Wang, Ying Wang, Xiao-Jun Zhao and Joan Ribas
Page 3926

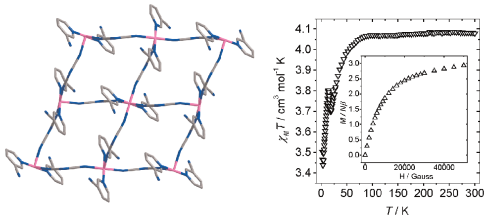

A series of new metal dicyanamide complexes with cyanopyridine terminal co-ligands have been prepared and structurally determined by X-ray single-crystal diffraction. The magnetic properties of the Co^{II} and Fe^{II} layered coordination polymers are also discussed.

Long-range antiferromagnetic ordering in $Cu_2NiB_2O_6$
Zhangzhen He, Tôru Kyômen, Tomoyasu Taniyama and Mitsuru Itoh
Page 3937

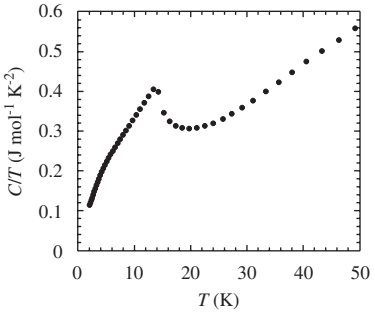

$Cu_2NiB_2O_6$ is found to display an antiferromagnetic phase transition at ~15 K, which differs from isostructural $Cu_2CoB_2O_6$ showing spin-glass behavior below 5 K. The nature of different magnetic ground states in these compounds can be understood by a non-equilateral triangle model.

Structure of sputtered Co–Se thin films prepared for an application in catalysis
L. Zhu, D. Susac, A. Lam, M. Teo, P.C. Wong, D. Bizzotto, S.A. Campbell, R.R. Parsons and K.A.R. Mitchell
Page 3942

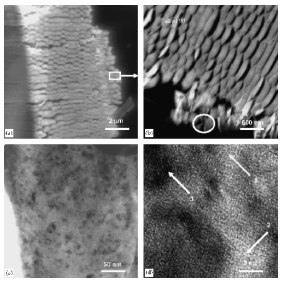

Sectioned sample of composition Co(44%)Se(56%) at progressively higher magnifications: (a) SEM image from area marked in Figure 1 of the full paper. The other images are from TEM. The rectangular area marked in (a) indicates the region magnified in (b): the area marked in (b) is magnified in (c) and (d).

Electronic polarizability and crystallization of K_2O–TiO_2–GeO_2 glasses with high TiO_2 contents
T. Fukushima, Y. Benino, T. Fujiwara, V. Dimitrov and T. Komatsu
Page 3949

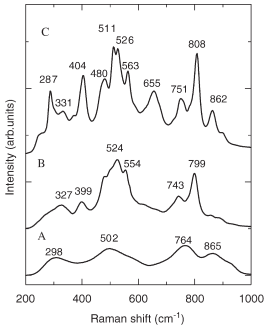

Raman scattering spectra at room temperature for A: 60KTG glass, B: crystallized (644 °C, 3 h) sample of KTG glass, and C: $K_2TiGe_3O_9$ crystalline phase prepared by a solid state reaction. 60KTG: $20K_2O$–$20TiO_2$–$60GeO_2$.

The non-centrosymmetric borate oxides, $MBi_2B_2O_7$ (M = Ca, Sr)
J. Barbier and L.M.D. Cranswick
Page 3958

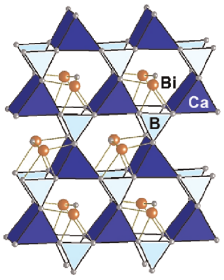

The new borate oxides, $MBi_2O(BO_3)_2$ (M = Ca, Sr), belong to the same layer structure-type built of MO_6 trigonal prisms, BO_3 triangles and Bi_2O groups.

Continued

Apparent giant dielectric constants, dielectric relaxation, and ac-conductivity of hexagonal perovskites $La_{1.2}Sr_{2.7}BO_{7.33}$ (B = Ru, Ir)
P. Lunkenheimer, T. Götzfried, R. Fichtl, S. Weber, T. Rudolf, A. Loidl, A. Reller and S.G. Ebbinghaus
Page 3965

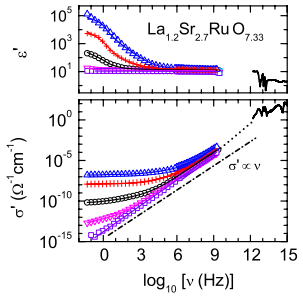

Frequency-dependent dielectric constant and conductivity of $La_{1.2}Sr_{2.7}RuO_{7.33}$ at various temperatures. A frequency range of more than 16 decades is covered, revealing giant values of the dielectric constant, hopping conduction, a superlinear power law of the conductivity, and phononic and electronic excitations in the infrared region.

Monoclinic phase of the misfit-layered cobalt oxide $(Ca_{0.85}OH)_{1.16}CoO_2$
Mitsuyuki Shizuya, Masaaki Isobe, Yuji Baba, Takuro Nagai, Yoshio Matsui and Eiji Takayama-Muromachi
Page 3974

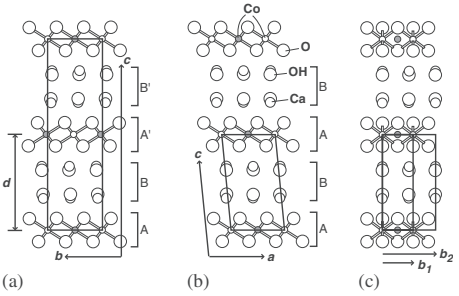

Crystal structure of two kinds of poly-type phases of the misfit-layered cobalt oxides $(Ca_{1-\delta}OH)_xCoO_2$: (a) projection along the a-axis of the orthorhombic structure; (b) projection along the b-axis of the monoclinic structure; and (c) projection along the [−1 0 0] direction of the monoclinic structure. In each case, the rectangle is the unit cell.

A new approach for the synthesis of K^+-free nickel hexacyanoferrate
Irene Carpani, Marco Giorgetti, Mario Berrettoni, Pier Luigi Buldini, Massimo Gazzano and Domenica Tonelli
Page 3981

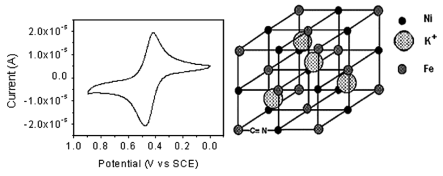

A new synthetic route is proposed to prepare a K^+-free nickel hexacyanoferrate by using a Ni,Al LDH, intercalated with $Fe(CN)_6^{3-}$, as host material. The different host–guest solubility allowed us to synthesize, with a quite good yield, a pure mixed hexacyanoferrate, which is very difficult to obtain. Elemental analysis and cyclic voltammetry confirmed the absence of K^+.

Mixed-metal flux synthesis of quaternary $RMn_2Tr_xZn_{20-x}$ compounds with Tr = Al, In
Evan M. Benbow and Susan E. Latturner
Page 3989

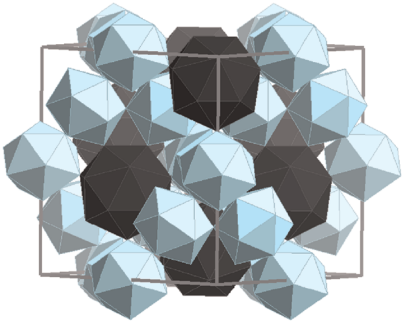

Crystals of new intermetallic phases $RMn_2Tr_xZn_{20-x}$ (Tr = Al or In; R = rare earth) were grown from Al/Zn or In/Zn flux mixtures. These compounds are quaternary variants of the $CeCr_2Al_{20}$ structure type. This structure can be viewed as a packing of polyhedra, as shown.

Photoluminescence: A probe for short, medium and long-range self-organization order in $ZrTiO_4$ oxide
Poty R. de Lucena, Edson Roberto Leite, Fenelon M. Pontes, Elson Longo, Paulo S. Pizani and José Arana Varela
Page 3997

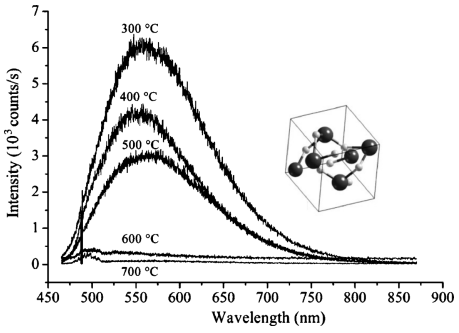

Photoluminescence as a probe to order level of the $ZrTiO_4$ oxide.

Three-dimensional molecular network, $[\{Cu(dps)_2(SO_4)\}\cdot 3H_2O\cdot DMF]_n$, and its different third-order NLO performance (dps = 4,4′-dipyridyl sulfide)
Yunyin Niu, Zhongjun Li, Yinglin Song, Mingsheng Tang, Benlai Wu and Xinquan Xin
Page 4003

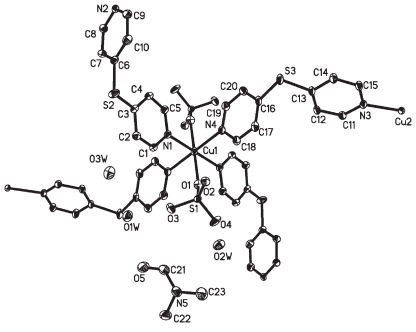

An ORTEP drawing of the asymmetric unit and the copper (II) coordination environment in **1**.

Structure refinement, dielectric, pyroelectric and Raman characterizations of $Ba_{1-x}La_{x(1-y)/2}Eu_{xy/2}Na_{x/2}TiO_3$ solid solution
Najmeddine Abdelmoula, Hamadi Khemakhem, Annie Simon and Mario Maglione
Page 4011

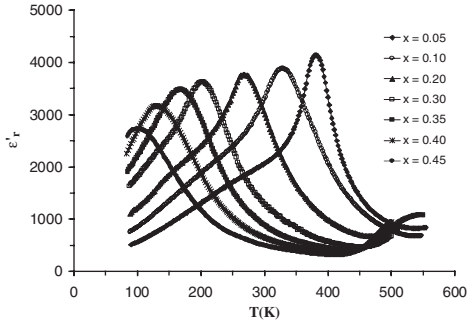

Temperature dependence of dielectric permittivity of $Ba_{1-x}La_{x(1-y)/2}Eu_{xy/2}Na_{x/2}TiO_3$ ($0 \leqslant x \leqslant 0.45$ and $xy = 0.04$) ceramics at 1 kHz.

Crystal structure of lanthanum bismuth silicate $Bi_{2-x}La_xSiO_5$ ($x \sim 0.1$)
Samuel Georges, François Goutenoire and Philippe Lacorre
Page 4020

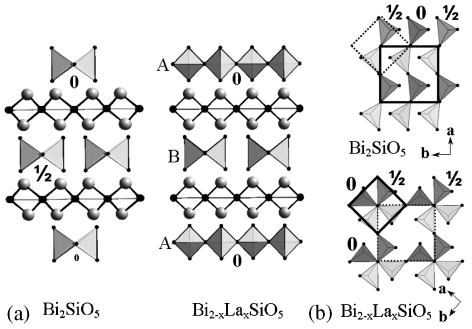

Structural relationships between Bi_2SiO_5 and $Bi_{2-x}La_xSiO_5$: (a) projection along a for Bi_2SiO_5, and along [110] for the local ordered description of $Bi_{2-x}La_xSiO_5$ and (b) projection along *c*.

U(IV)/Ln(III) mixed site in polymetallic oxalato complexes. Part III: Structure of $Na[Yb(C_2O_4)_2(H_2O)] \cdot 3H_2O$ and the derived quadratic series $(NH_4^+)_{1-x}[Ln_{1-x}U_x(C_2O_4)_2(H_2O)] \cdot (3+x)\ H_2O$, *Ln* = Y, Pr–Sm, Gd, Tb
B. Chapelet-Arab, L. Duvieubourg, G. Nowogrocki, F. Abraham and S. Grandjean
Page 4029

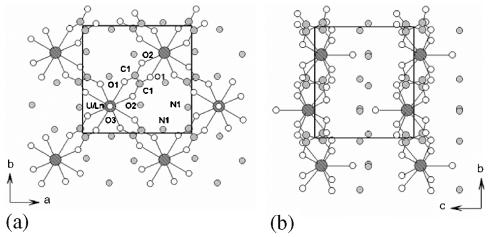

Crystal structure of the quadratic U(IV)/Ln(III) oxalates.

Hydrothermal synthesis, crystal structure and luminescence of four novel metal–organic frameworks
Yi-Shan Song, Bing Yan and Zhen-Xia Chen
Page 4037

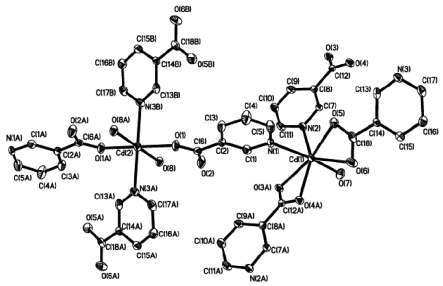

Using the principle of crystal engineering, four novel metal-organic coordination polymers, $\{[Cd^1(nic)_2(H_2O)]_2[Cd^2(nic)_2(H_2O)_2]\}_n$, $[Cd_2(fma)_2(phen)_2]_n$, $[Cd(fma)(bipy)(H_2O)]_n$ and $[Zn(mal)(bipy) \cdot 3H_2O]_n$ have been synthesized by hydrothermal method. X-ray analysis reveals that complex **1** possesses an unprecedented two-dimensional topology structure constructed from three-ply-like layers, complex **2** is an infinite 2D undulating network, complexes **3** and **4** belong to a 1D chain. The results indicate a transformation of fumarate into malate during the course of hydrothermal treatment of complex 4.

Rapid Communications

UV–VUV-excited photoluminescence of *RE*-activated $CaLaP_3O_{10}$ (*RE* = Eu,Tb)
Chunfang Wu, Yuhua Wang and Wenjing Liu
Page 4047

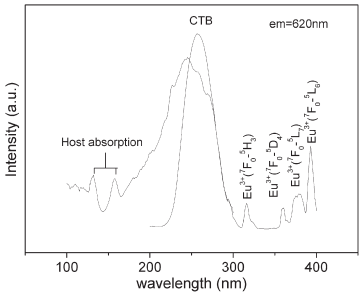

Excitation spectra of $CaLa_{0.85}P_3O_{10}$:$0.15Eu^{3+}$ ($\lambda_{em} = 620$ nm).

Ferroelectric perovskite-type barium copper niobate: $BaCu_{1/3}Nb_{2/3}O_3$
W. Zhang, N. Kumada, Y. Yonesaki, T. Takei, N. Kinomura, T. Hayashi, M. Azuma and M. Takano
Page 4052

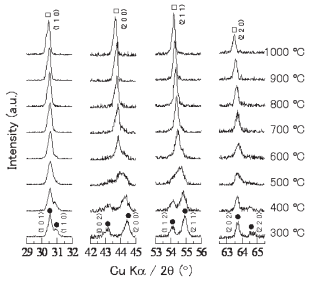

High temperature X-ray powder diffraction of perovskite-type $BaCu_{1/3}Nb_{2/3}O_3$.

Continued

Evaluation of the initial growth of electroless deposited Co(W,P) diffusion barrier thin film for Cu metallization
Aaron Zhu, Yossi Shacham-Diamand and Mark Teo
Page 4056

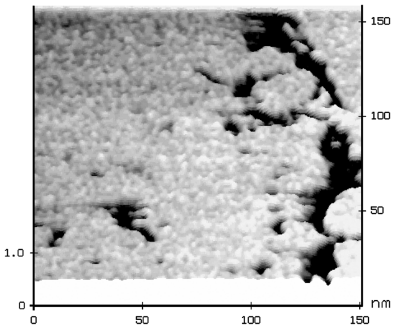

Strong lateral coalescence of Co(W,P) nuclei after 3 s deposition.

Author Index for Volume 179 ***Page 4066***

Cumulative Keyword Index ***Page 4075***

Author inquiries

Submissions

For detailed instructions on the preparation of electronic artwork, consult Elsevier's Author Gateway at http://authors.elsevier.com.

Other inquiries

Visit Elsevier's Author Gateway (http://authors.elsevier.com) for the facility to track accepted articles and set up e-mail alerts to inform you of when an article's status has changed. The Author Gateway also provides detailed artwork guidelines, copyright information, frequently asked questions and more.

Contact details for questions arising after acceptance of an article, especially those relating to proofs, are provided after registration of an article for publication.

Language Polishing
Authors who require information about language editing and copyediting services pre- and post-submission should visit http://www.elsevier.com/wps/find/authorshome.authors/languagepolishing or contact authorsupport@elsevier.com for more information. Please note Elsevier neither endorses nor takes responsibility for any products, goods, or services offered by outside vendors through our services or in any advertising. For more information please refer to our Terms & Conditions at http://www.elsevier.com/wps/find/termsconditions.cws_home/termsconditions.

For a full and complete Guide for Authors, please refer to *J. Solid State Chem.,* Vol. 179, Issue 8, pp. *bmi–bmv*. The instructions can also be found at http://www.elsevier.com/wps/find/journaldescription.cws_home/622898/authorinstructions.

Journal of Solid State Chemistry has no page charges.